Sensors and Materials, Vol. 34, No. 12 (2022) 4289–4305
MYU Tokyo

S & M 3111

Land-cover Classification and Change Assessment for Shijiazhuang City, North China, during 1987–2020 Based on Remote Sensing

Shi-Kai Song,[1,2,3] Lei-Bin Wang,[1,2,3] Qiang Liu,[2] and Yuan-Jie Zhao[2*]

[1]Postdoctoral Research Station of Geography, Hebei Normal University, Shijiazhuang, Hebei 050024, China
[2]School of Geographical Sciences, Hebei Normal University, Shijiazhuang, Hebei 050024, China
[3]Hebei Technology Innovation Center for Remote Sensing Identification of Environmental Change, Shijiazhuang, Hebei 050024, China

(Received June 8, 2022; accepted August 9, 2022)

Keywords: Shijiazhuang City, land cover, Landsat, greening

High-accuracy and high-resolution land-cover datasets are crucial for city planning and sustainable development. In recent decades, Shijiazhuang City has experienced significant land use/cover changes resulting from economic development, population growth, and urban expansion. However, few studies have been reported on land-cover datasets over Shijiazhuang City, which has a complex topography and a heterogeneous landscape. In this study, single- and multi-temporal Landsat images over Shijiazhuang City were classified by random forest, support vector machine, and classification and regression tree classifiers based on 382 field survey samples; their accuracies were assessed through a comparison with two other land-cover datasets (GlobeLand30-2020 and GLC_FCS30-2020). Land-cover dynamics from 1988 to 2020 and greening trends from 2000 to 2020 were determined. The results show that the classification of multi-temporal images with spectral and phenological characteristics using random forest classifiers achieved the highest overall accuracy of 86.4% in comparison with 69.6 and 47.5% for GlobeLand30-2020 and GLC_FCS30-2020, respectively. From 1988 to 2020, the impervious surfaces and deciduous broad-leaved forest regions in the study area expanded, while irrigated cropland and shrubland areas decreased gradually. From 2000 to 2020, the normalized difference vegetation index (NDVI) of natural vegetation types in urban and mountainous areas significantly increased ($p < 0.05$), while the greenness of the entire study area and irrigated cropland regions exhibited no significant changes. In this paper, we provide useful information for research into city land-cover classification and assessment, along with ecological environment protection and planning.

1. Introduction

Land-cover changes can significantly affect land-surface energy balances, ecological systems, earth–atmosphere coupling, and sustainable development.[1,2] Long duration, high-resolution, and accurate land-cover mapping and monitoring through remote sensing are crucial

*Corresponding author: e-mail: ecoenvir@163.com
https://doi.org/10.18494/SAM3988

ISSN 0914-4935
https://myukk.org/

datasets for agricultural and forestry management, ecological environment protection, disaster prevention and mitigation, urban planning, and national monitoring.[3]

Many factors—such as the quality of remote sensing images, methods, and samples—affect the accuracy and efficiency of land-cover classification. In recent years, machine learning has been widely applied in the field of land-cover mapping, including the random forest, support vector machine, decision tree, and neural network.[4,5] Studies have shown that random forest classifiers have relatively high classification accuracies,[6,7] especially in areas with complex topographies.[8]

In areas with complex environments and fragmented landscapes, the spectral characteristics of ground objects are often disordered, and the phenomena of "the same object with the same spectrum" and "the same object with a different spectrum" are common, so land-cover mapping in such areas is challenging.[5] In comparison with single-temporal remote sensing images, time-series images can facilitate repeated observations and fully exploit the spectral and phenological information of vegetation, significantly improving the classification performance.[9,10] Furthermore, it has also been found that more temporal images lead to higher accuracies.[11,12]

Acquiring a high-precision land-cover map also depends on the high quality of training and validation datasets.[13] When using machine-learning classifiers, classification results are highly sensitive to the number, type ratio, and spatial autocorrelation of the training data.[14] However, in-site observation samples require significant manpower and time to collect. Therefore, in some studies, samples were directly selected from Google Earth high-resolution images or Landsat images according to prior knowledge.[4,15] However, these image samples could inevitably lead to errors because of the different times of data collection and the prevalence of spectrally similar classes, among other factors.[16]

Different computing platforms have different data filtering, processing, computing, and storing performances, which further affect the scope and efficiency of land-cover mapping.[17] In comparison with a single machine, local workstation, or server, the Google Earth Engine (GEE) cloud platform can more efficiently filter, process, and classify long time-series remote sensing imagery from the block to the global scale.[17,18]

Shijiazhuang, the capital city of Hebei Province, is located in the central and southern parts of Hebei Province, with the Taihang Mountains to the west and the North China Plain to the east. In recent decades, Shijiazhuang has experienced significant land-cover change due to rapid industrialization and urbanization, along with economic development. Furthermore, the ecological and environmental problems in this region are severe, and include water shortages, high temperatures, heat waves, and air pollution.[19] Although it is imperative to map and access changes in local land cover, there is limited research on this issue because of the highly heterogeneous and complex landscape in transition zones between mountains and plains, in addition to cloudy remote sensing images during the growth season of land vegetation. Xiao *et al.* investigated the temporal and spatial changes in Shijiazhuang land use from 1987 to 2001 using multisource remote sensing and geographic information systems.[20] Wu *et al.* detected the spatiotemporal patterns of urbanization in Shijiazhuang using Landsat images from 1980 to 2010.[21] However, none of the aforementioned groups analyzed the rapid changes in Shijiazhuang over the past decade, and the applicability of the two publicly published global land-cover datasets—GlobeLand30[22] and GLC_FCS30[23]—over Shijiazhuang is unknown.

Sun *et al.* found that large cities in China displayed significant greening from 2001 to 2018.[24] In recent years, along with rapid expansion and drastic changes in land use/cover, significant landscape engineering has been conducted in Shijiazhuang.[25,26] However, the combined effects of urban expansion and landscape engineering on city greening changes are unknown.

Landsat imagery with a 30 m spatial resolution from 1984 to the present is a suitable data source for mapping long-term land cover in Shijiazhuang. On the basis of these considerations, in this work, we intend to map and assess the 30 m land cover of Shijiazhuang based on Landsat images and observation samples from 1988 to 2020 using the GEE platform. The classification accuracies of single and multiple images were evaluated using three machine learning classifiers, and two public global land-cover datasets were compared. A local greening trend was detected based on moderate resolution imaging spectroradiometer (MODIS) normalized difference vegetation index (NDVI) from 2000 to 2020.

2. Materials and Methods

2.1 Study area

The study area (37°42’–38°20′N and 114°5′–114°56′E) is located east of the Taihang Mountains and west of the North China Plain. The landform comprises hills with a height of 1500 m and plains with a height of 80 m from west to east, leading to a complicated terrain and a heterogeneous landscape [Figs. 1(a) and 1(b)]. The research area covers a size of about 5200 km^2,

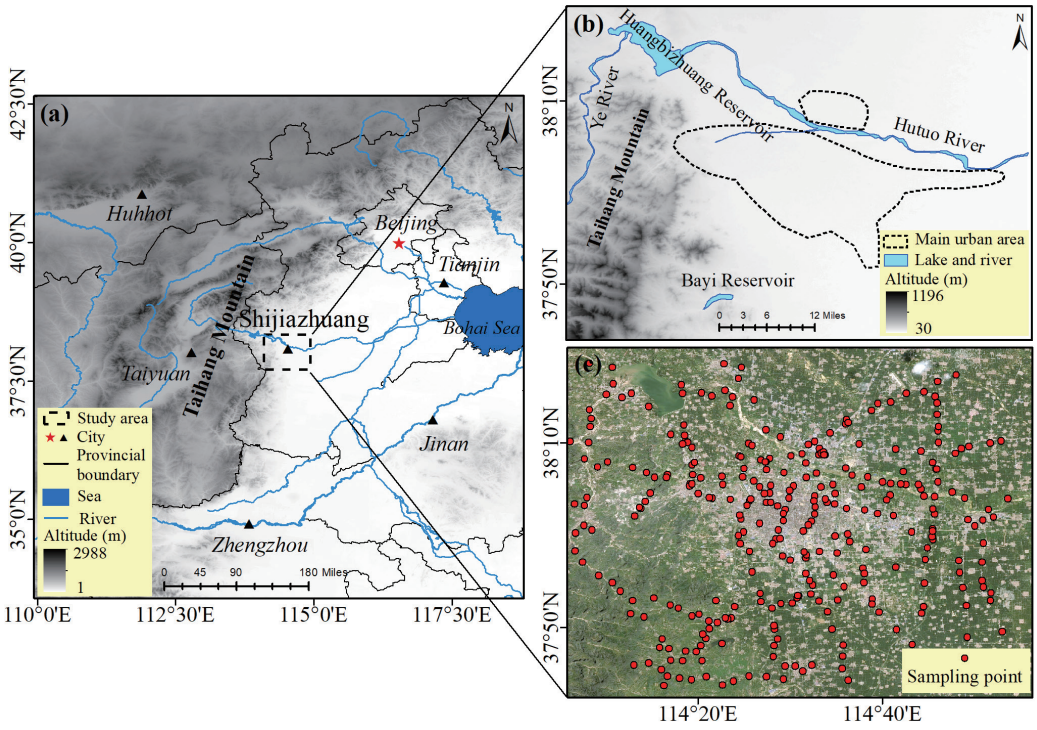

Fig. 1. (Color online) Study area and distribution of sampling points.

consisting of the main urban area and outer suburbs of Shijiazhuang, with the main urban area located at the center. Huangbizhuang Reservoir is in the northwest, Hutuo River in the north, and a large orchard in the southeast of the city [Figs. 1(a) and 1(b)]. The climate is primarily a typical warm temperate continental monsoon climate; Shijiazhuang City has a hot and rainy summer and a cold and dry winter, as shown in Fig. 2. The main land-cover types in the region include woodlands, grasslands, shrublands, cultivated land, artificial impervious surfaces, and water. As the capital of Hebei Province, Shijiazhuang City is a hub for politics, culture, transportation, and economics. Since the reform and opening up of China, Shijiazhuang has experienced rapid industrialization and urbanization along with economic development, particularly over the last 20 years, and the urban area has expanded significantly.[19]

2.2 Data

The Landsat-8 Operational Land Image surface reflectance tier 1 (Landsat-8 OLI SR T1) data and Landsat-5 Thematic Mapper surface reflectance tier 1 (Landsat-5 TM SR T1) data from the GEE cloud storage were adopted for classification. The SR datasets have been atmospherically corrected using the Landsat Surface Reflectance Code (LaSRC) algorithm. The blue, green, red, near-infrared (NIR), and short-wave infrared (SWIR-1 and SWIR-2) spectral bands of the Landsat-8 OLI (denoted as B2–B7) and the blue, green, red, NIR, SWIR-1, and SWIR-2 spectral bands of the Landsat-5 TM (denoted as B1–B5, B7) were considered in the analysis. Previous studies have shown that different remote sensing indices are sensitive to different types of land cover. Thus, there is no general index that covers all land-cover types,[27] and indices are not considered in this research.

Owing to a long observation period of 16 days and the local rainy summer conditions, there were few cloudless images during the vegetation growth season (from March to October). The GEE platform was utilized to quickly search, query, display, and filter cloudless or less cloudy high-quality images. 1988, 1997, 2004, 2011, and 2020 were determined as the target years, with no less than eight high-quality images in the entire year, and five in the growth season. Images

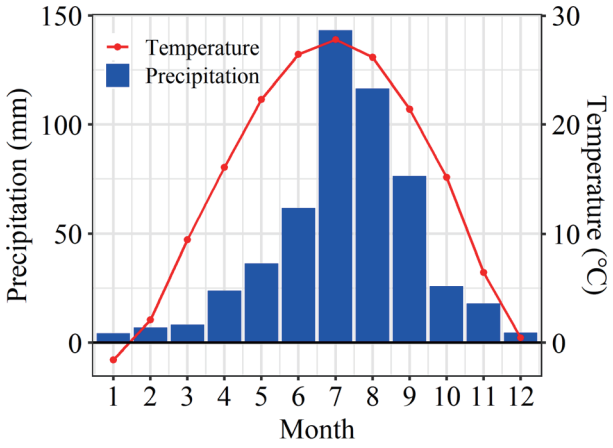

Fig. 2. (Color online) Monthly mean temperature and precipitation.

in the target year are a combination of images of over three years, including the preceding and following years (e.g., images from 2010 to 2012 were used for producing the year 2011 mosaic).

The annual maximum NDVI of Landsat images cannot adequately reflect the optimal growth status of vegetation in one year because of the 16-day observation period and fewer high-quality images. The combined MODIS NDVI during the observation period is more conducive to capturing the changes in vegetation growth status. Therefore, MODIS NDVI (MODIS/006/MOD13Q1) with a 16-day observation period and a 250 m spatial resolution from the GEE database was adopted to analyze the changes in vegetation greenness from 2000 to 2020. We employed the 30 m digital elevation model (DEM) generated from the Shuttle Radar Topography Mission (SRTM).

Two publicly released global land-cover datasets are used—GlobeLand30[22] (http://www.globallandcover.com) and GLC_FCS30[23] (https://zenodo.org/record/4280923). GlobeLand30, one of the most widely used global land-use/land-cover datasets, with a resolution of 30 m, was developed by using the pixel-object-knowledge-based (POK-based) algorithm for the three periods of data in 2000, 2010, and 2020. Moreover, the overall classification accuracy of GlobeLand30-2020 is 85.72% on the global scale, based on more than 230000 validation sample points.[22] The global 30-m land-cover product (GLC_FCS30-2020) with a fine classification system was produced in the GEE platform by combining time-series data of Landsat imagery, the global prior training dataset, and local adaptive random forest model, which was validated to have an overall global accuracy of 82.5% based on 44,043 validation sample points.[23] GLC_FCS30-2020 was further released after the optimization of GLC_FCS30-2015 by combining multisource auxiliary datasets and prior expert knowledge.[23]

2.3 Methods

2.3.1 Samples and land-cover classification system

Owing to certain errors in simple image sampling, a total of 382 samples were collected and organized through an in situ field survey and image referencing, and the requirements for ground surveys are as follows: (1) typical, homogeneous land cover with a radius greater than 150 m; (2) ground objects that remained unchanged from 1988 to 2020, according to the historical images of Google Earth and Landsat, for example, sturdy trees for forest samples, old buildings or roads for impervious surfaces, and large shrub areas in high-altitude regions for shrubland. In total, 382 sample points [Fig. 1(c)] and nine types of land cover are retained, including 28 rainfed cropland samples, 57 irrigated cropland samples, 22 deciduous broad-leaved forest samples, 12 evergreen needle-leaved forest samples, 42 shrubland samples, 280 grassland samples, 100 samples of impervious surfaces, 15 samples of bare areas, and 30 water samples. Typical sample pictures are given in Fig. 3. Seventy percent of these sample points are randomly separated as training samples, with 30% as verification samples.

Land cover focuses on the physical properties of land surface objects, such as forest, grassland, farmland, desert, and artificial impervious surfaces, while land use places emphasis on describing the purpose and application of these surface objects and includes commercial

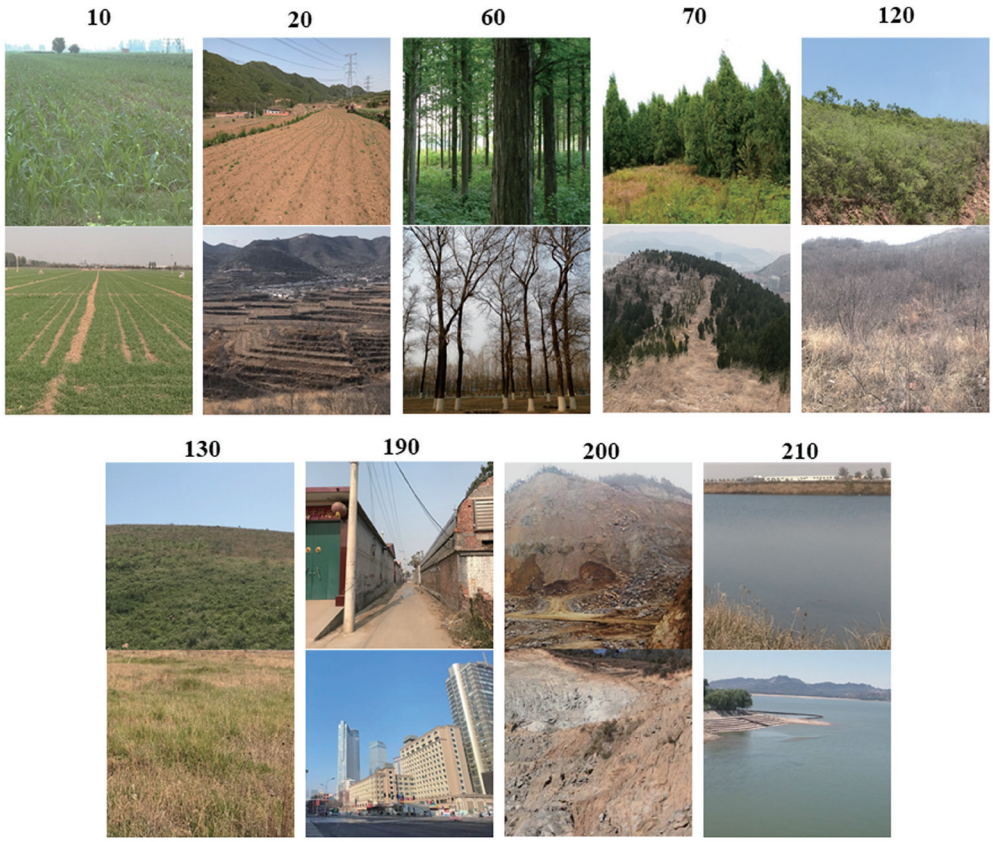

Fig. 3. (Color online) Photos of typical sample areas. Numbers indicate the codes of land-cover classes.

areas, residential areas, roads, canals, and fish ponds. The 30 m resolution remote sensing data used in this paper is more suitable for the classification of land cover rather than land use. Therefore, on the basis of the Land Cover Classification System (LCCS) from the Food and Agriculture Organization (FAO) of the United Nations[28] and the classification of GLC_FCS30,[23] land cover in Shijiazhuang was categorized into nine types (Table 1).

2.3.2 Classification and accuracy assessment

Three kinds of pixel-based machine learning classifiers provided by GEE, namely, random forest, support vector machine, and classification, and regression trees were applied with default parameters. Three groups of comparative experiments were designed, each of which corresponds to a classifier. Each group includes single- and multi-temporal image (a combination of single-temporal images in a year) classification tests.

A confusion matrix was calculated with the overall accuracy and Kappa coefficient to quantitatively assess the accuracy of the classification maps. Slightly different classification results were generated because of the random selection of sample points, even if the same classifier with the same classification parameters was used.[7,9] To overcome this instability, each

Table 1
Land-cover classes and definitions.

Code	Class	Description
10	Rainfed cropland	Mainly distributed in mountainous areas with no irrigation facilities. The main crop is corn, which is usually sown after a heavy rain in the period from April to June and harvested in September and October.
20	Irrigated cropland	Mainly distributed in the plain; the farming mode is two crop rotations a year: corn and wheat. Corn is sown in June and is harvested in October, followed by winter wheat, which is sown in June of the following year.
60	Deciduous broad-leaved forest	Distributed in mountainous plains and covered by poplar, willow, elm, locust, apple, pear, peach, plum, apricot, walnut, and chestnut.
70	Evergreen needle-leaved forest	Pine and cypress.
120	Shrubland	*Zizyphus jujuba* and *Vitex negundo var. heterophylla*.
130	Grassland	Natural and artificial grasslands covered by annual herbs.
190	Impervious surfaces	Land for urban and rural residents; transportation, industrial, and mining facilities.
200	Bare areas	Sandy, bare rock, gravel, etc.
210	Water bodies	Artificial reservoirs, lakes, rivers, ponds, etc.

experiment was conducted 10 times to generate a mean value as the final result. Classification and assessments were implemented on the GEE platform.

2.3.3 Regional greening analysis

On the basis of land-cover maps and DEM data, the study area was divided into three sub-regions: the main urban area, natural vegetation areas in mountainous regions, and cultivated land in plain regions. The temporal and spatial variations of greening were analyzed in accordance with MODIS NDVI (MOD13Q1) from 2000 to 2020.

The research process in this study is as follows. (1) Using GEE, the random forest, support vector machine, and classification decision tree classifiers were applied to classify the single- and multi-temporal images of Landsat-8 for the year 2020 using 382 measured samples, and the accuracy of the classification results (SLC30-2020) was evaluated to determine the optimal method to be used. (2) SLC30-2020 was compared with two other public global land-cover datasets (GlobeLand30 and GLC_FCS30). (3) Using GEE, the best classification method was utilized to map the land cover in the years 1988, 1997, 2004, and 2011, and quantitative changes in land cover were ascertained. (4) Dynamic spatial patterns of MODIS NDVI were analyzed from 2000 to 2020.

3. Results and Discussion

3.1 Spectral features of different types of land cover

In 2020, eight Landsat-8 high-quality images were used (January 31, March 3, April 4, May 22, August 10, September 7, October 13, and December 30). Spectral reflectance information was extracted from images on the basis of the field samples, and the multi-temporal spectral

reflectance curves of different land types are illustrated in Figs. 4 and 5. Figure 4 shows three types of nonvegetated land types, namely, impervious surfaces, bare areas, and water body, with a significant difference between band reflectance and small seasonal variations. The reflectance of impervious surfaces was the highest, followed by those of bare areas and water bodies.

Figure 5 shows six vegetation land types, namely, rainfed cropland, irrigated cropland, deciduous broad-leaved forest, evergreen needle-leaved forest, shrub, and grassland. The B5 band was the most sensitive to the vegetation growth status, and its reflectance was proportional to the growth status. The B6 and B7 bands were more sensitive and inversely proportional to this status, and the B2–4 band was less sensitive to it.

In irrigated cropland, corn is harvested and wheat is sown in October, and it has a low vegetation coverage, which significantly differed from the other five types of vegetation in terms of the spectral reflectance curve. Moreover, irrigated land was mainly distributed in the plain areas, which was easy to distinguish and classify. Rainfed cropland, deciduous broad-leaved

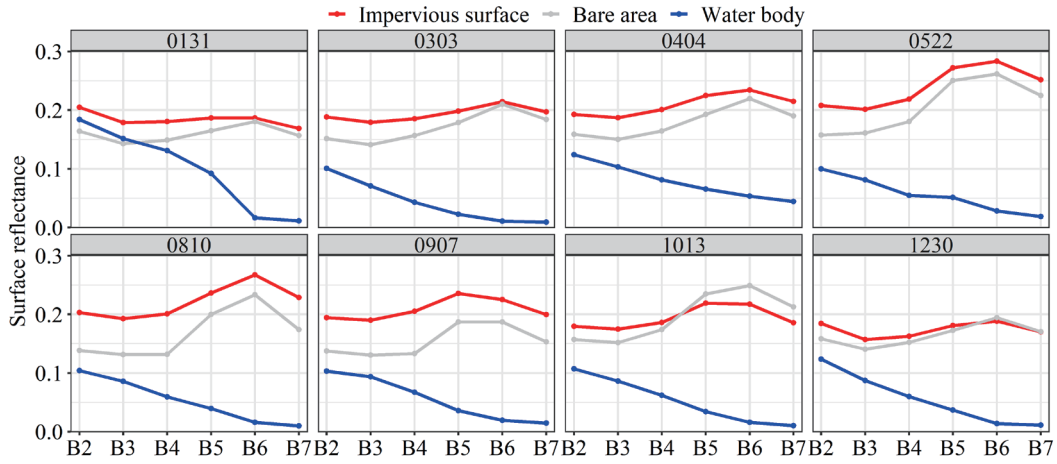

Fig. 4. (Color online) Spectral features of nonvegetated land cover.

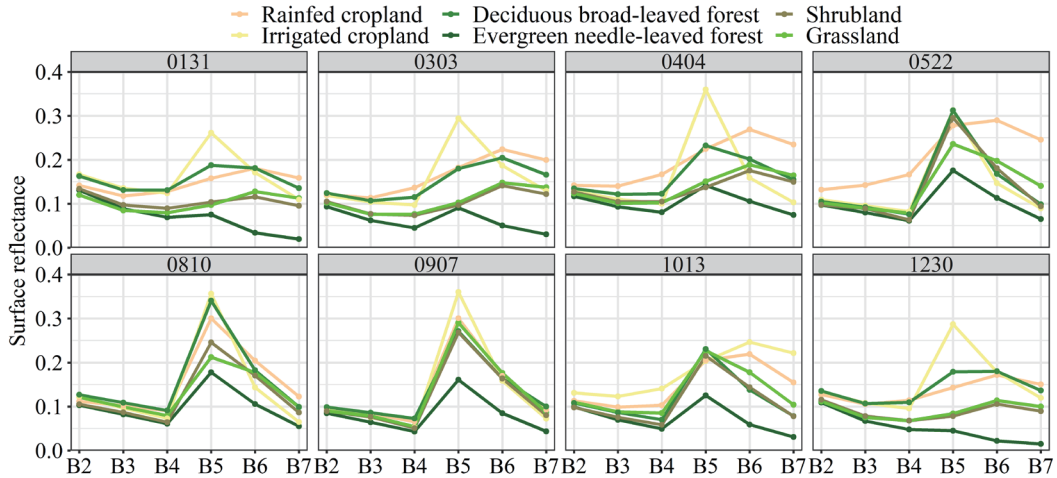

Fig. 5. (Color online) Spectral features of vegetated land cover.

forest, evergreen needle-leaved forest, shrub, and grassland were the main vegetation types which often distribute crossly in mountainous areas, with similar band characteristics and obvious growth seasons. Before April, the natural vegetation types (deciduous broad-leaved forest, evergreen needle-leaved forest, shrub, and grassland) were all in the early growing season, and the spectral characteristics were similar. In May, the natural vegetation grew rapidly, while the rainfed cropland corn was just sown or soon to be sown, with low vegetation coverage. The reflectance of the bands differed from that of the natural vegetation. The band reflectance of the deciduous broad-leaved forest was the lowest in the entire year, and the seasonal difference was small, so it was easy to distinguish from other natural vegetation. The reflectance of all bands of deciduous broad-leaved forests was significantly higher than that in the shrub and grassland during the nongrowing season. The spectral reflectance curves of shrub and grassland were too similar to distinguish and exhibited certain differences only in band B5–7 in May (Fig. 5).

The spectral features of impervious surfaces, bare areas, water bodies, and irrigated cropland differed greatly and could be easily classified on the basis of a single-temporal image. Rainfed cropland, deciduous broad-leaved forest, evergreen needle-leaved forest, shrub, and grassland had obvious growth seasons, and their spectral information was similar. In contrast to a single-temporal image, multi-temporal images could distinguish the phenological differences between vegetation types.

3.2 Land-cover classification and evaluation

In 2020, 33 comparative tests among three groups were designed, with each group including eight single-temporal and three multi-temporal image combinations, referred to as combination_1 (“April 4 + October 13”), combination_2 (“April 4 + May 22 + October 13”), and combination_3 (all of the eight single images). April 4 presents the initial stages of vegetation growth, May 22 is between the initial growth and the lush period, and October 13 is the transition period between the lush and the declining period. On these three days, the spectral differences of landscape types were obvious, which was conducive to classification. The accuracies of the 33 tests are given in Table 2.

Among the single-temporal image classifications, April 4 exhibited the highest overall accuracy, which could be due to the obvious differences in the initial growth conditions of different vegetation types. On September 7, all types of vegetation were in their lush growth state, with the highest vegetation coverage and the smallest differences in band reflectance, leading to the lowest classification accuracy. The accuracy of multi-temporal combination_1 was higher than those of all single-temporal classification results, while that of combination_2 was higher, and that of combination_3 was the highest. Among the three classifiers, random forest had the highest classification accuracy overall, while support vector machine and decision classification tree differed only slightly. Taking combination_3 as an example, the classification overall accuracies of random forest, support vector machine, and decision classification tree reached 86.9, 80.8, and 80.5%, and those of Kappa coefficients were 0.84, 0.77, and 0.79, respectively. In summary, the spectrum- and phenology-based “random forest +

Table 2
Overall accuracies and Kappa coefficients of 33 tests.

Images	Random forest		Support vector machine		Classification and regression trees	
	Overall accuracy	Kappa coefficient	Overall accuracy	Kappa coefficient	Overall accuracy	Kappa coefficient
0131	77.7	73.4	68.6	62.8	67.0	59.8
0303	80.4	76.3	76.8	72.6	75.2	69.6
0404	80.8	77.5	78.6	74.8	75.4	70.2
0522	79.4	75.8	73	68.6	69.2	62.4
0810	73.1	70.3	65.7	60.6	67.9	60.9
0907	72.6	69.6	65.5	61.3	67.4	61.3
1013	74.5	69.5	67.8	62	68.2	61.8
1230	74.8	70.1	67.6	61.7	67.9	60.9
Combination_1	81.9	78.4	76.2	72.2	76.6	71.8
Combination_2	85.0	81.7	78.8	74.4	79.4	75.2
Combination_3 All	86.9	84.2	80.8	77.2	83.8	80.8

combination_3" approach presented competitive performance in terms of mapping and producing Shijiazhuang_Landcover_30-2020 (SLC30-2020), which is shown in Fig. 6(a).

Combining previous findings with our results,[11,12] we found that multi-temporal images could significantly improve the classification performance, and more temporal images result in higher accuracies. For classifiers, several studies have shown that the random forest algorithm is more suitable than other classifiers for the supervised classification of time-series images, which is consistent with the findings of previous studies.[29,30]

3.3 Comparison with GlobeLand30 and GLC_FCS30

To better reflect the product quality, we compared our mapping results with those from other available land-cover datasets. The SLC30-2020, GlobeLand30-2020, and GLC_FCS30-2020 datasets over this study area are shown in Fig. 6. On the basis of 382 field-based observations, the overall and single-category accuracies were evaluated, as presented in Table 3.

SLC30-2020 has the highest overall accuracy at 86.9%. For single images, easily discernible spectral information (Fig. 5) resulted in relatively high accuracies (>90%) of water body, impervious surfaces, irrigated land, and evergreen needle-leaved forest. Rainfed cropland, broad-leaved deciduous forest, shrub, and grassland had lower accuracies (>73%) owing to similar spectral features and a mixed distribution. The main classification uncertainties were as follows: a part of mountain shadows was wrongly classified as evergreen coniferous forest and water body, and misclassifications commonly occurred between bare areas and impervious surfaces (Table 3).

The overall accuracy of GlobeLand30-2020 reached 80.6%. The cropland and forest were only classified as Level 1, rainy and irrigable cropland were categorized as cropland, and evergreen needle-leaved forest and deciduous broad-leaved forest were classified as forest. The

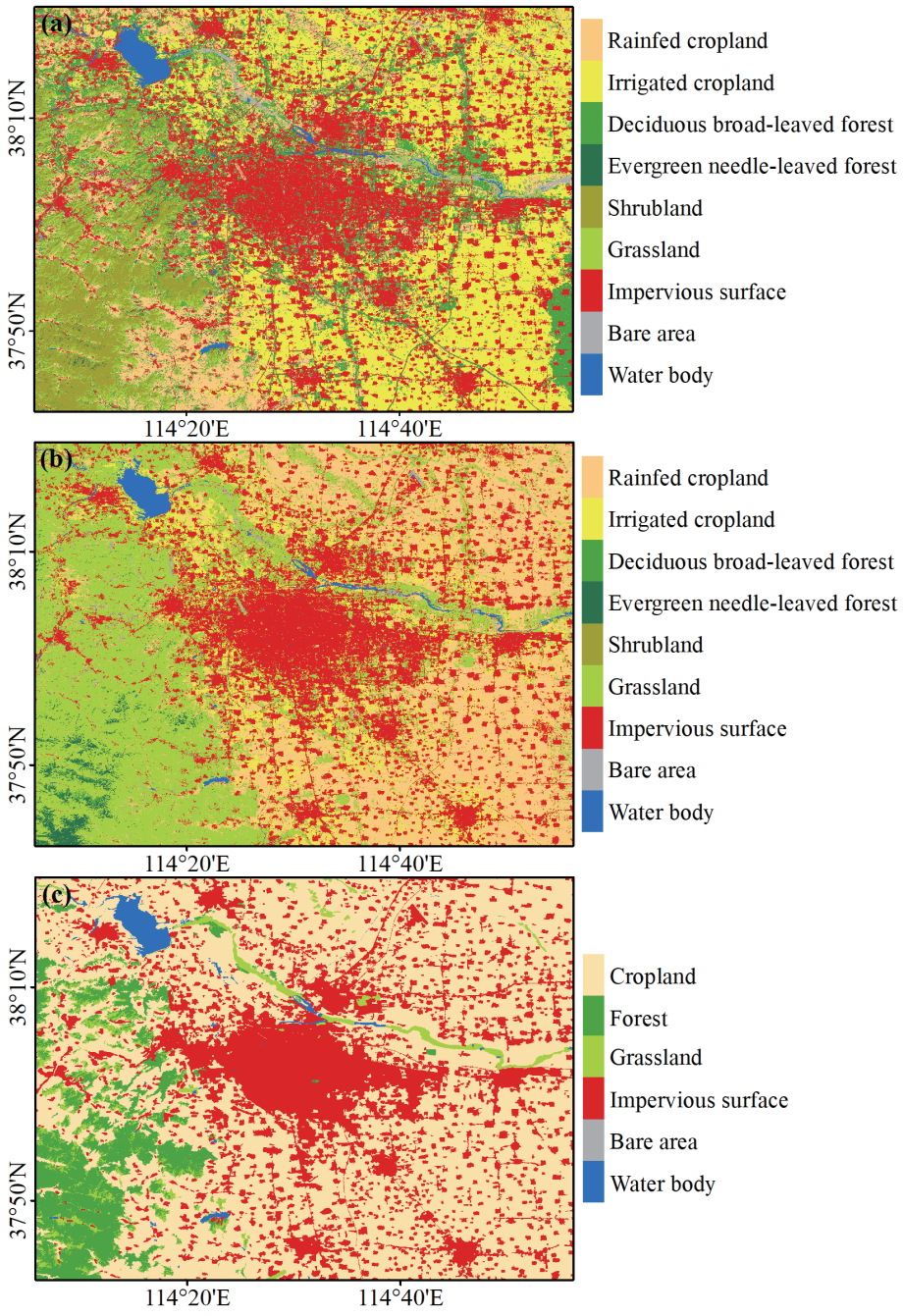

Fig. 6. (Color online) Land-cover maps of SLC30-2020, GlobeLand30-2020, and GLC_FCS30-2020.

cropland was widely distributed in both plain and mountainous areas, with an accuracy exceeding 96%, which could be related to its widespread distribution. In mountainous areas, shrubs were actually the dominant vegetation, with the largest distribution area; however, all of the shrubland was misclassified as cropland and forest (18%) (Table 3).

Table 3
Overall accuracies and Kappa coefficients of three land-cover datasets.

Code	Type	SLC30-2020	GLC_FCS30-2020	GlobeLand30-2020
10	Rainfed cropland	73.6	2.9	96.2
20	Irrigated cropland	98.4	28.4	
60	Deciduous broad-leaved forest	79.7	1.3	18
70	Evergreen needle-leaved forest	90.5	33.3	
120	Shrubland	82.1	0	—
130	Grassland	77.6	82.2	31.1
190	Impervious surfaces	96.4	91.5	97.2
200	Bare areas	68.5	50.6	2.9
210	Water body	97.2	96.1	60
All types of land cover		86.9	47.5	69.6

The overall accuracy of GLC_FCS30-2020 was 47.5%, which was the lowest value among the three datasets. In terms of classes, the accuracies for water bodies, impervious surfaces, and grasslands were 96.1, 91.5, and 82.2%, respectively. In mountainous areas, most shrubs were misclassified as grasslands, leading to a low accuracy of 3.7%. The irrigated land, which was widely distributed in the plain area, was misclassified as rainy cropland, while the rainfed cropland–which was one of the main vegetation types in the mountain regions–was missed. Thus, the classification accuracies of rainy and irrigated cropland were only 2.9 and 28.4%, respectively. Highway forest belts in the eastern region and orchards (apple, pear, peach, etc.) in the southeast were misclassified as cropland, resulting in a forest accuracy of 33.3% (Table 3). The above analysis indicates that the proposed SLC30-2020 outperformed other similar datasets over the Shijiazhuang region.

3.4 Land-cover changes from 1988 to 2020

Landsat images over Shijiazhuang in 1988, 1997, 2004, and 2011 were classified by the proposed "random forest + combination_3" method using the GEE platform, and mapping results with high overall accuracies (>82%) were analyzed to quantify the land-cover dynamics.

In 1988, 1997, 2004, 2011, and 2020, the areas of impervious surfaces were 718, 870, 1068, 1297, and 1750 km^2, respectively, exhibiting a gradually increasing trend, with a total gain of 1032 km^2 over 30 years (Fig. 7). The main transition form was the outward expansion of the main urban areas and outer suburban counties, covering the original cropland and shrubland (Fig. 8). Primarily transformed from irrigated cropland–in the form of greening projects along the northern Hutuo River and new green belts along main roads in the east and new large orchards in the southeast–the deciduous broad-leaved forest area increased from 373 km^2 in 1988 to 1111 km^2 in 2020 (Figs. 7 and 8). Conversely, the irrigated cropland area in the plain gradually decreased by 1475 km^2, decreasing from 3237 km^2 in 1988 to 1762 km^2 in 2020. In the mountains, the shrubland area decreased by 338 km^2 over 30 years. There was no significant change in other land types (Fig. 7).

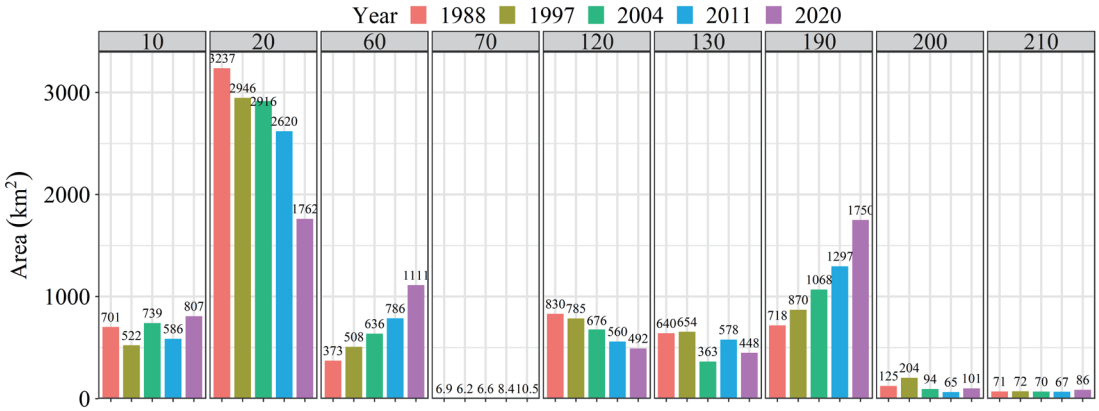

Fig. 7. (Color online) Statistics regarding land-cover changes in 1988, 1997, 2004, 2011, and 2020.

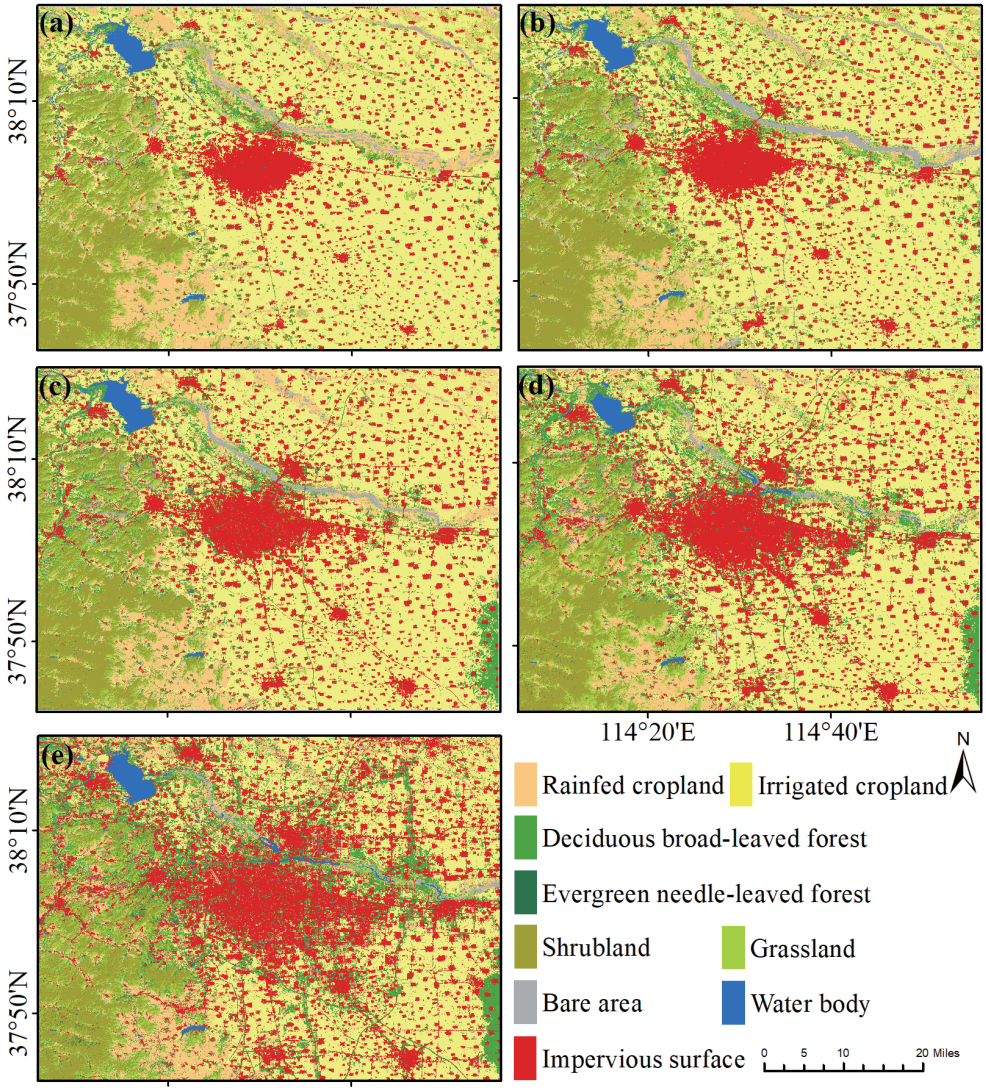

Fig. 8. (Color online) Land-cover changes in 1988, 1997, 2004, 2011, and 2020.

To conclude the quantitative analysis, over Shijiazhuang, the areas of impervious surfaces and forest land increased, while irrigated land and shrubland areas decreased. Wu *et al.* found that the Shijiazhuang urban area expanded significantly;[21] moreover, several greening projects were carried out, especially over the past 10 years, and a large number of parks and green spaces were built.[25,26]

3.5 Greening changes from 2000 to 2020

MODIS's annual maximum NDVI in the main urban area was between 0 and 0.2 in 2000 [Fig. 9(a)]. In 2020, the main urban area expanded significantly, and the NDVI increased to between 0.3 and 0.5, indicating significant greenness [Fig. 9(b)]. As can be seen from Fig. 9(c), the NDVI in the old urban area increased from 2000 to 2020, while that in the new outspread urban areas decreased. This is because the old urban area had constantly been implementing greening projects, and the new outspread urban area overtook cropland, but the greening project had not yet been implemented. Most of the western mountainous areas also experienced a greening trend, and the bare areas in the upper reaches of the Hutuo River were gradually replaced by vegetation; therefore, the NDVI also exhibited an increasing trend [Fig. 9(c)].

According to the DEM and classification results for SLC30-2020, the study area can be divided into the mountainous natural vegetation area (more than 150 m above sea level, and land cover is forest, shrublands, or grassland), plain irrigated cropland area, and central urban area.

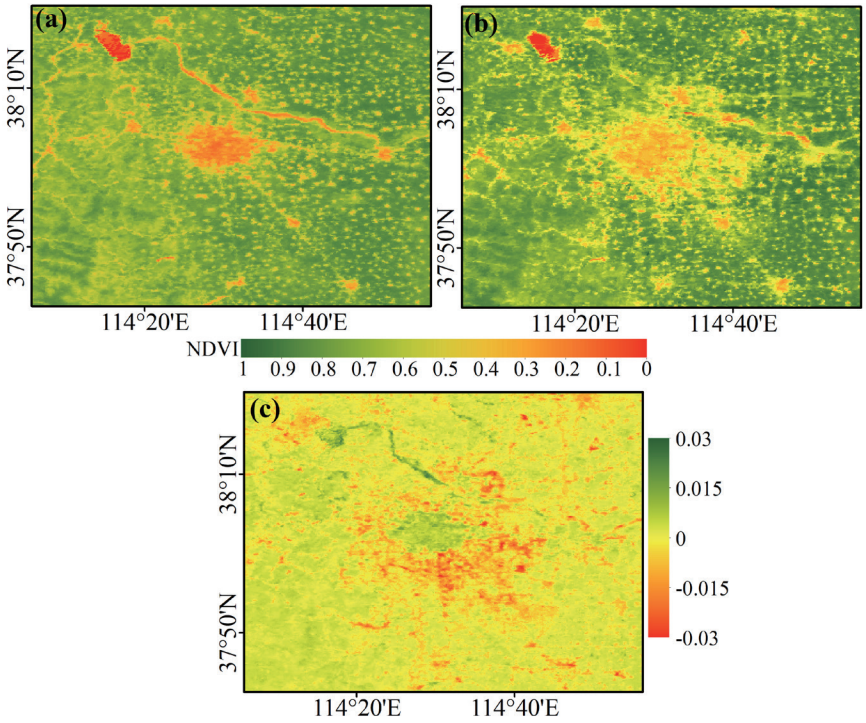

Fig. 9. (Color online) Spatial distribution and changes in annual maximum NDVI from 2000 to 2020: (a) spatial distribution for 2000, (b) spatial distribution for 2020, and (c) trend from 2000 to 2020.

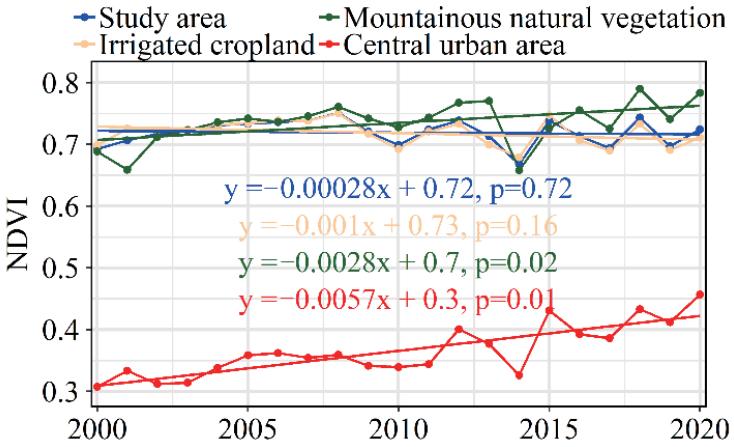

Fig. 10. (Color online) Variation trends of NDVI in different regions from 2000 to 2020.

From 2000 to 2020, the NDVI over the natural vegetation in mountainous areas and the central urban areas increased significantly ($p < 0.05$), while the greenness of the entire area and irrigated cropland region did not change significantly (Fig. 10).

The greening trend of mountainous natural vegetation was consistent with the overall trend in China over recent years. China has been implementing ambitious programs to mitigate land degradation and planting trees to tackle air pollution and climate change.[31] Combining the results of previous studies[24,32,33] with the results of this study has shown that some cities are experiencing long-term expansion and continuous greening.

4. Conclusions

In summary, the main conclusions of this paper are as follows.

(1) The spectral features of the impervious water surfaces, bare areas, and water body differed significantly, making them easy to distinguish. Irrigated land, which was under anthropogenic management, could be easily identified. Rainfed cropland, deciduous broad-leaved forest, evergreen needle-leaved forest, shrubland, and grassland had similar band reflectance characteristics. In contrast to single-temporal images, multi-temporal images could distinguish phenological differences among land-cover types.

(2) Random forest, support vector machine, and classification decision tree classifiers were applied to classify the single- and multi-temporal images. Test results indicate that the "random forest + combination_3" method was the most competitive strategy.

(3) The overall classification accuracies of SLC30-2020, GLC_FCS30-2020, and GlobeLand30-2020 are 86.9, 47.5, and 69.6%, respectively.

(4) According to the dynamics of land cover in 1988, 1997, 2004, 2009, and 2020, the areas of impervious surfaces and deciduous broad-leaved forests increased gradually; irrigated cropland and shrubland areas declined gradually in the plain and mountain areas, and there was no significant change in other land types.

(5) From 2000 to 2020, the natural vegetation in mountainous areas and the NDVI in the main urban area of Shijiazhuang increased significantly ($p < 0.05$), while the irrigated cropland region and the entire study area exhibited no significant changes.

In this study, we not only demonstrated the feasibility of the multi-temporal image classification algorithm using random forest classifiers based on the spectral and phenological characteristics in the GEE platform, but also enriched the land-cover maps of the Shijiazhuang region. In future research, the mapping accuracy of vegetation types in mountainous areas needs to be improved, and the driving factors of natural vegetation greening in mountainous regions need to be further analyzed.

Acknowledgments

This research was supported by the Natural Science Foundation of Hebei Province (Grant No. D2021205013), Science Foundation of Hebei Normal University (Grant No. L2018B23), and National Natural Science Foundation of China (Grant No. 41877448).

References

1 G. C. Hurtt, L. P. Chini, S. Frolking, R. A. Betts, J. Feddema, G. Fischer, J. P. Fisk, K. Hibbard, R. A. Houghton, A. Janetos, C. D. Jones, G. Kindermann, T. Kinoshita, K. Klein Goldewijk, K. Riahi, E. Shevliakova, S. Smith, E. Stehfest, A. Thomson, P. Thornton, D. P. van Vuuren, and Y. P. Wang: Clim. Change **109** (2011) 117. https://doi.org/10.1007/s10584-011-0153-2

2 J. A. Foley, R. DeFries, G. P. Asner, C. Barford, G. Bonan, S. R. Carpenter, F. S. Chapin, M. T. Coe, G. C. Daily, H. K. Gibbs, J. H. Helkowski, T. Holloway, E. A. Howard, C. J. Kucharik, C. Monfreda, J. A. Patz, I. C. Prentice, N. Ramankutty, and P. K. Snyder: Science **309** (2005) 570. https://doi.org/10.1126/science.1111772

3 J. Liu, W. Kuang, Z. Zhang, X. Xu, Y. Qin, J. Ning, W. Zhou, S. Zhang, R. Li, C. Yan, S. Wu, X. Shi, N. Jiang, D. Yu, X. Pan, and W. Chi: J. Geogr. Sci. **69** (2014) 3. https://doi.org/10.1007/s11442-014-1082-6

4 X. Luo, X. H. Tong, and H. Y. Pan: IEEE Trans. Geosci. Remote Sens. **59** (2021) 1029. https://doi.org/10.1109/tgrs.2020.2999558

5 F. Zhang and X. J. Yang: Remote Sens. Environ. **251** (2020) 14. https://doi.org/10.1016/j.rse.2020.112105

6 P. Duong Cao, T. Ta Hoang, T. Van Thinh, and K. N. Nasahara: Geocarto Int. **37** (2021) 4053. https://doi.org/10.1080/10106049.2021.1878292

7 M. Calderón-Loor, M. Hadjikakou, and B. A. Bryan: Remote Sens. Environ. **252** (2021) 112148. https://doi.org/10.1016/j.rse.2020.112148

8 X. Gu, X. Gao, H. Ma, F. Shi, X. Liu, and X. Cao: Remote Sens. Technol. Appl. **34** (2019) 57. http://www.rsta.ac.cn/CN/10.11873/j.issn.1004-0323.2019.1.0057

9 L. A. Qu, Z. J. Chen, M. C. Li, J. J. Zhi, and H. M. Wang: Remote Sens. **13** (2021) 23. https://doi.org/10.3390/rs13030453

10 X. Zhang, X. M. Xiao, X. X. Wang, X. Xu, B. Q. Chen, J. Wang, J. Ma, Z. Bin, and B. Li: Remote Sens. Environ. **247** (2020) 14. https://doi.org/10.1016/j.rse.2020.111916

11 S. Zhang, Z. Li, F. Xu, J. Pan, X. Jiang, and W. Zhang: Chin. J. Ecol. **39** (2020) 3174. http://www.cje.net.cn/CN/10.13292/j.1000-4890.202009.015

12 J. Chen, X. Wei, Y. Liu, Q. Min, R. Liu, W. Zhang, and C. Guo: Remote Sens. Technol. Appl. **35** (2020) 1226. http://rsta.ac.cn/article/2020/1004-0323/1004-0323-2020-35-5-1226.shtml

13 C. Pelletier, S. Valero, J. Inglada, N. Champion, C. Marais Sicre, and G. Dedieu: Remote Sens. **9** (2017) 173. https://doi.org/10.3390/rs9020173

14 K. Millard and M. Richardson: Remote Sens. **7** (2015) 8489. https://doi.org/10.3390/rs70708489

15 H. Liu, P. Gong, J. Wang, X. Wang, G. Ning, and B. Xu: Remote Sens. Environ. **258** (2021) 112364. https://doi.org/10.1016/j.rse.2021.112364

16 G. M. Foody and A. Mathur: Remote Sens. Environ. **103** (2006) 179. https://doi.org/10.1016/j.rse.2006.04.001

17 M. Amani, A. Ghorbanian, S. A. Ahmadi, M. Kakooei, A. Moghimi, S. M. Mirmazloumi, S. H. A. Moghaddam, S. Mahdavi, M. Ghahremanloo, S. Parsian, Q. Wu, and B. Brisco: IEEE J. Sel. Top. Appl. Earth Obs. Remote Sens. **13** (2020) 5326. https://doi.org/10.1109/JSTARS.2020.3021052
18 J. Dong, W. Kuang, and J. Liu: Sci. Chin. Earth Sci. **48** (2018) 259. https://doi.org/10.1007/s11430-017-9143-3
19 J. Shao and J. Ge: J. Urban Plann. Dev. **146** (2020) 13. https://doi.org/10.1061/(asce)up.1943-5444.0000619
20 J. Y. Xiao, Y. J. Shen, J. F. Ge, R. Tateishi, C. Y. Tang, Y. Q. Liang, and Z. Y. Huang: Landsc. Urban Plann. **75** (2006) 69. https://doi.org/10.1016/j.landurbanplan.2004.12.005
21 W. J. Wu, S. Q. Zhao, C. Zhu, and J. L. Jiang: Landsc. Urban Plann. **134** (2015) 93. https://doi.org/10.1016/j.landurbplan.2014.10.010
22 J. Chen, J. Chen, A. P. Liao, X. Cao, L. J. Chen, X. H. Chen, C. Y. He, G. Han, S. Peng, M. Lu, W. W. Zhang, X. H. Tong, and J. Mills: ISPRS-J. Photogramm. Remote Sens. **103** (2015) 7. https://doi.org/10.1016/j.isprsjprs.2014.09.002
23 X. Zhang, L. Liu, X. Chen, Y. Gao, S. Xie, and J. Mi: Earth Syst. Sci. Data Discuss. **2020** (2020) 1. https://doi.org/10.5194/essd-2020-182
24 L. Sun, J. Chen, Q. Li, and D. Huang: Nat. Commun. **11** (2020) 1. https://doi.org/10.1038/s41467-020-19158-1
25 Z. Dong: Hebei Forestry **1** (2021) 17. http://lycy.hebei.gov.cn/journal_3733.html#book7/page18-page19
26 J. Zhang and J. Tuo: Hebei Forestry **23** (2019) 22. http://lycy.hebei.gov.cn/menu/show.php?pid=3166
27 V. Rodriguez-Galiano and M. Chica-Olmo: Appl. Geogr. **35** (2012) 208. https://doi.org/10.1016/j.apgeog.2012.06.014
28 A. Di Gregorio: Land Cover Classification System: Classification Concepts and User Manual: Lccs **2** (Food & Agriculture Org., 2005).
29 X. Chai, M. Li, Y. Zhou, J. Wang, and Q. Tian: Remote Sens. Technol. Appl. **35** (2020) 315. http://www.rsta.ac.cn/CN/10.11873/j.issn.1004-0323.2020.2.0315
30 C. Gómez, J. C. White, and M. A. Wulder: ISPRS-J. Photogramm. Remote Sens. **116** (2016) 55. https://doi.org/10.1016/j.isprsjprs.2016.03.008
31 C. Chen, T. Park, X. H. Wang, S. L. Piao, B. D. Xu, R. K. Chaturvedi, R. Fuchs, V. Brovkin, P. Ciais, R. Fensholt, H. Tommervik, G. Bala, Z. C. Zhu, R. R. Nemani, and R. B. Myneni: Nat. Sustain. **2** (2019) 122. https://doi.org/10.1038/s41893-019-0220-7
32 K. Yang, W. Sun, Y. Luo, and L. Zhao: J. Environ. Manage. **291** (2021) 9. https://doi.org/10.1016/j.jenvman.2021.112598
33 S. Q. Zhao, S. G. Liu, and D. C. Zhou: PNAS **113** (2016) 6313. https://doi.org/10.1073/pnas.1602312113

About the Authors

Shi-Kai Song received his Ph.D. degree from Xinjiang Institute of Ecology and Geography, Chinese Academy of Sciences in 2017, and is now working at the School of Geographical Sciences, Hebei Normal University. He is member of the Geographical Society of China. His research interests are in applications of remote sensing. (songsk@hebtu.edu.cn)

Lei-Bin Wang received his Ph.D. degree from Beijing Normal University in 2020, and is now working at the School of Geographical Sciences, Hebei Normal University. His research interests are in applications of remote sensing and climate change. (leibin.wang@hebtu.edu.cn)

Qiang Liu received his Ph.D. degree from Wuhan University in 2014, and is now working at the School of Geographical Sciences, Hebei Normal University. His research interests are in applications of remote sensing and hydrology. (qiangliu@hebtu.edu.cn)

Yuan-Jie Zhao is a professor in the School of Geographical Sciences, Hebei Normal University. He received his Ph.D. degree from Shenyang Institute of Applied Ecology, Chinese Academy of Sciences in 2001. His research interests include applications of remote sensing and regional ecology and environment. (ecoenvir@163.com)